Laser-Printed Plasmonic Metasurface Supporting Bound States in the Continuum Enhances and Shapes Infrared Spontaneous Emission of Coupled HgTe Quantum Dots

Sergeeva, Kseniia A.; Pavlov, Dmitrii V.; Seredin, Albert A.; Mitsai, Eugeny V.; Sergeev, Aleksandr A.; Modin, Evgeny B.; Sokolova, Anastasiia V.; Lau, Tsz Chun; Baryshnikova, Kseniia V.; Petrov, Mihail I.; Kershaw, Stephen V.; Kuchmizhak, Aleksandr A.; Wong, Kam Sing; Rogach, Andrey L.

Published in:
Advanced Functional Materials

Published: 25/10/2023

Document Version:
Post-print, also known as Accepted Author Manuscript, Peer-reviewed or Author Final version

Published version (DOI):
10.1002/adfm.202307660

Publication details:
Sergeeva, K. A., Pavlov, D. V., Seredin, A. A., Mitsai, E. V., Sergeev, A. A., Modin, E. B., Sokolova, A. V., Lau, T. C., Baryshnikova, K. V., Petrov, M. I., Kershaw, S. V., Kuchmizhak, A. A., Wong, K. S., & Rogach, A. L. (2023). Laser-Printed Plasmonic Metasurface Supporting Bound States in the Continuum Enhances and Shapes Infrared Spontaneous Emission of Coupled HgTe Quantum Dots. *Advanced Functional Materials*, *33*(44), Article 2307660. https://doi.org/10.1002/adfm.202307660

Laser-Printed Plasmonic Metasurface Supporting Bound States in the Continuum Enhances and Shapes Infrared Spontaneous Emission of Coupled HgTe Quantum Dots

Kseniia A. Sergeeva[1†], Dmitrii V. Pavlov[2†], Albert A. Seredin[3†], Eugeny V. Mitsai[2], Aleksandr A. Sergeev[2,4], Evgeny B. Modin[5], Anastasiia V. Sokolova[1], Tsz Chun Lau[6], Kseniia V. Baryshnikova[3], Mihail I. Petrov[3], Stephen V. Kershaw[1], Aleksandr A. Kuchmizhak[2,7*], Kam Sing Wong[4], Andrey L. Rogach[1]**

K. A. Sergeeva, A. V. Sokolova, Dr. S. V. Kershaw, Prof. A. L. Rogach
Department of Materials Science and Engineering, and Centre for Functional Photonics (CFP), City University of Hong Kong, Hong Kong SAR, 999077 PR China
E-mail: andrey.rogach@cityu.edu.hk

Dr. D. V. Pavlov, Dr. E. V. Mitsai, Dr. A. A. Sergeev, Dr. A. A. Kuchmizhak
Institute of Automation and Control Processes of the FEB RAS, 5 Radio St., 690041 Vladivostok, Russia
E-mail: alex.iacp.dvo@mail.ru

A. A. Seredin, Dr. K. V. Baryshnikova, Dr. M. I. Petrov
School of Physics and Engineering, ITMO University, Saint-Petersburg, 197101, Russia
Email: m.petrov@metalab.ifmo.ru

Dr. A. A. Sergeev, Prof. K. S. Wong
Department of Physics, Hong Kong University of Science and Technology, Clear Water Bay Rd, Kowloon, Hong Kong SAR, 999077, PR China

Dr. E. B. Modin
CIC NanoGUNE BRTA, Avda Tolosa 76, Donostia-San Sebastian, 20018, Spain

Dr. T. C. Lau
Department of Physics, City University of Hong Kong, Hong Kong SAR, 999077, PR China

Dr. A. A. Kuchmizhak
Pacific Quantum Center, Far Eastern Federal University, Vladivostok, 690922, Russia

K. A. Sergeeva, Dr. D.V. Pavlov, A. A. Seredin
[†]These authors contributed equally to the work

Keywords: infrared-emitting quantum dots, photoluminescence enhancement, metasurface, plasmonic array, bound states in the continuum

Abstract

In order to advance the development of quantum emitter-based devices, it is essential to enhance light-matter interactions through coupling between semiconductor quantum dots with high quality factor resonators. Here, we demonstrate efficient tuning of the emission properties of HgTe quantum dots in the infrared spectral region by coupling them to a plasmonic metasurface that supports bound states in the continuum. The plasmonic metasurface, composed of an array of gold nanobumps, was fabricated using single-step direct laser printing, opening up new opportunities for creating exclusive 3D plasmonic nanostructures and advanced photonic devices in the infrared region. We observed a 12-fold enhancement of the photoluminescence in the 900-1700 nm range under optimal coupling conditions. By tuning the geometry of the plasmonic arrays, we achieved controllable shaping of the emission spectra, selectively enhancing specific wavelength ranges across the emission spectrum. The observed enhancement and shaping of the emission are attributed to the Purcell effect, as corroborated by systematic measurements of radiative lifetimes and optical simulations based on the numerical solution of Maxwell's equations. Moreover, coupling of the HgTe photoluminescence to high quality factor modes of the metasurface improves emission directivity, concentrating output within a ~20° angle.

1. Introduction

The rapid advancement of optoelectronic devices can be largely attributed to the availability of high-quality quantum emitters. Colloidal quantum dots (QDs), in particular, have transitioned from laboratories to real-world devices, becoming one of the most promising classes of materials.[1] Unlike fluorescent dyes, QDs can exhibit narrow and readily tunable emission spectra, making them well-suited for applications which require pure, bright, and stable emission spanning the whole range from the visible to infrared (IR) wavelengths.[1] Near- and mid-IR spectral ranges are of special practical interest, where inexpensive quantum emitters exhibiting high photoluminescence (PL) quantum yield (QY) are in high demand for the realization of photodetectors, direct optical sensors, security systems, remote thermodetectors, spectrometers, and so on.[2] However, the performance of existing IR-emitting QDs is largely

limited by the dominance of non-radiative recombination channels, while the efficiency of radiative channels decreases at the longer wavelengths in accordance with Fermi's golden rule.

To address these issues, researchers have focused on both refining synthetic methods of producing IR-emitting QDs[3] and enhancing the QDs' interaction with pump irradiation by optimizing device architectures.[4] Coupling of emitters to resonant structures (i.e., planar arrangements of nanoantennas) generally leads to several competitive processes, including (i) the increase of the exciton radiative recombination rate (and therefore a reduction of the exciton radiative lifetime) due to the Purcell effect,[5a,b] (ii) enhancement of the excitation efficiency by localized electromagnetic near-fields and modification of the radiation directivity,[5c,d] and (iii) acceleration of nonradiative recombination because of plasmon-induced energy transfer.[5e] The balance between these competing processes is needed to develop various functional devices, primarily those operating in the visible and near-IR spectral range.[5d, 6a] In particular, for longer wavelengths covering telecommunication bands (1360-1625 nm), demonstrations of efficient control over QD's PL remain scarce,[6b, 6c] owing to the complexity of realizing nanoantennas that provide simultaneous matching of the visible-range excitation and IR-range emission bands of the coupled QDs. Inexpensive fabrication and replication of such optically resonant nanostructures on device-level scales still pose challenges, as they are primarily reliant on costly and non-scalable lithography-based techniques.[6d] In addition, methods of production of these resonant structures need the flexibility to be readily compatible with the overall device structures that they are to be integrated with.

Recently, the field of nanophotonics has witnessed a surge of periodically arranged resonant nanostructures supporting bound states in the continuum (BIC).[7] These states, characterized by a destructive interference of modes in properly designed nanostructures, allow for nearly complete cancellation of radiative losses, leading to theoretically unlimited quality factors (Q-factors) of the resonant modes.[7d] In realistic systems, factors such as roughness, structure disordering, and finite sizes prevent the complete elimination of radiative losses turning ideal BIC modes into quasi-BIC (qBIC) ones.[7a] As a result, reported Q-factors remain limited, albeit significantly high, accompanied by a strong local enhancement of the electromagnetic (EM) field amplitude. The remarkable properties of qBIC-supporting structures have already been harnessed in a variety of photonic applications, paving the way for next-generation sensing,[8a, 8b] active light-emitting devices,[8c] and nonlinear optical devices.[8d, 8e, 8f] In particular, plasmonic structures supporting BIC modes present multiple advantages over dielectric-based resonant systems, such as improved field confinement, intensified light-matter interactions, and increased versatility.[9] These benefits call for the development of their large-scale fabrication

and compatibility with solution-processing technologies, thereby transitioning from proof-of-concept experiments to the development and evaluation of practical devices, such as high-efficiency, narrowband IR light sources.

In this work, we extended studies started previously[6b] on coupling near-IR emitting HgTe QDs to plasmonic metasurfaces. Through step-by-step optimization of excitation conditions and coupling efficiency, performed together with numerical simulations we have found that the plasmonic metasurface used supports qBIC modes, which efficiently tune the output PL from the QD monolayer. Specifically, when a QD monolayer is deposited on a plasmonic metasurface with an optimized dielectric spacer thickness of 10 nm between them and is excited via higher than 0.65 numerical aperture optics, whilst the qBIC mode spectrally matches the PL maximum, we demonstrate that over an order of magnitude stronger signal and a narrowing of the emission spectrum is obtained. The observed enhancement and emission spectrum shaping are attributed to the Purcell effect, as corroborated by systematic measurements of the radiative lifetimes and numerical simulations.

2. Results and Discussions

Near-IR emitting HgTe QDs with an average size (h_{QD}) of 3.2 nm and 3.6 nm and narrow size distribution (Figure S1a, b) were synthesized according to our previously reported method (details are given in the Experimental section). The plasmonic metasurface was composed of gold nanoresonators arranged in a square-shaped lattice, that interacts with a deposited monolayer of HgTe QDs upon photoexcitation (**Figure 1a**). In some measurements, a thin (10-40 nm) Al_2O_3 dielectric layer was used to separate the metasurface from the QD monolayer and prevent PL quenching effects when the emitters were in close proximity to the patterned gold layer. The metasurface consisted of hollow surface elevations (referred to as nanobumps) with nanoscale protrusions on top (referred to as nanojets) produced on the Au thin film surface using direct fs laser printing.[38] The ablation-free formation mechanism of the Au nanobumps upon laser exposure, which involves ultrafast melting and deformation of the Au film, ensured remarkably good reproducibility of the nanoresonators' geometry within the array (Figure 1b). The simplicity of this lithography-free fabrication procedure stands for the scalability of the fabrication process towards producing plasmonic arrays of mm-scale extent, which is crucial for device realization.

Properly arranged nanobumps have been previously shown to support a collective plasmonic mode with a resonant wavelength λ_R, which can be tuned by both lattice period Λ and the nanobump geometry (Figure S3).[10b, 10c, 10d] The latter can be tailored by the applied pulse

fluence and the laser beam profile (proportional to $1.22\lambda/NA$),[10b, 11] in turn providing a flexible way to adjust the spectral position of this collective resonance of the plasmonic array with respect to the emission band (with a central wavelength of λ_{PL}) of the HgTe QDs. This is illustrated in Figure 1c (solid curve under the shaded area), which displays the Fourier transmission infrared spectroscopy (FTIR) reflection spectrum of the nanobump array (Λ = 900 nm) with a collective plasmon mode, $\lambda_R \sim$ 1320 nm, that spectrally matches the PL band of the HgTe QDs. Notably, depositing the Al_2O_3 dielectric spacer on top of the nanobump Au array linearly redshifts the spectral position of the mentioned mode due to changes in the local refractive index. Even though the maximal Al_2O_3 thickness used is this study is 40 nm, we have checked the dependence of λ_R on the deposited layer thickness (d) in a much broader range and found it equal to $\Delta\lambda_R \sim$ 2 nm per 1 nm of deposited spacer layer at least up to d = 200 nm (Figure S4a). This feature reflects the plasmonic nature of the collective mode and provides an alternative method to calibrate the AFM- and XPS-verified thicknesses of both the dielectric and QD layers applied (Figure S4b) via the observed red shifts in the mode position.

The collective mode signatures observed in FTIR measurements were also fully reproduced in numerical simulations, which confirmed that these modes are of the BIC type.[7a] Indeed, while their dispersion lies above the light cone (Figure S5), these modes are poorly coupled to free space modes and, in the vicinity of the Γ-point, appear completely uncoupled from the radiative continuum, becoming bounded due to the symmetry of the metasurface.[7b] The field distributions of both the lateral electric field components (E_x and E_y) exhibit the asymmetric character typical for BIC modes (insets in Figure 1e).[12] The BIC nature of the modes is also evident in the reflection spectrum of the metasurface plotted for varied angles of incidence in the TM geometry (Figure 1d). The features of resonant reflection disappear as soon as one approaches the Γ-point, which stems from the absence of radiative losses at the Γ-point and the related divergence of the radiative Q-factor (Q_{rad}) of the BIC modes shown in Figure 1e (see Supporting Information Section 4 for simulation details). The non-radiative Q-factor (Q_{nr}) slowly varies close to the Γ-point giving a contribution to the total Q-factor (Q_{tot}) (see also Section 4 in Supporting Information file):

$$\frac{1}{Q_{tot}} = \frac{1}{Q_{rad}} + \frac{1}{Q_{nr}}.$$

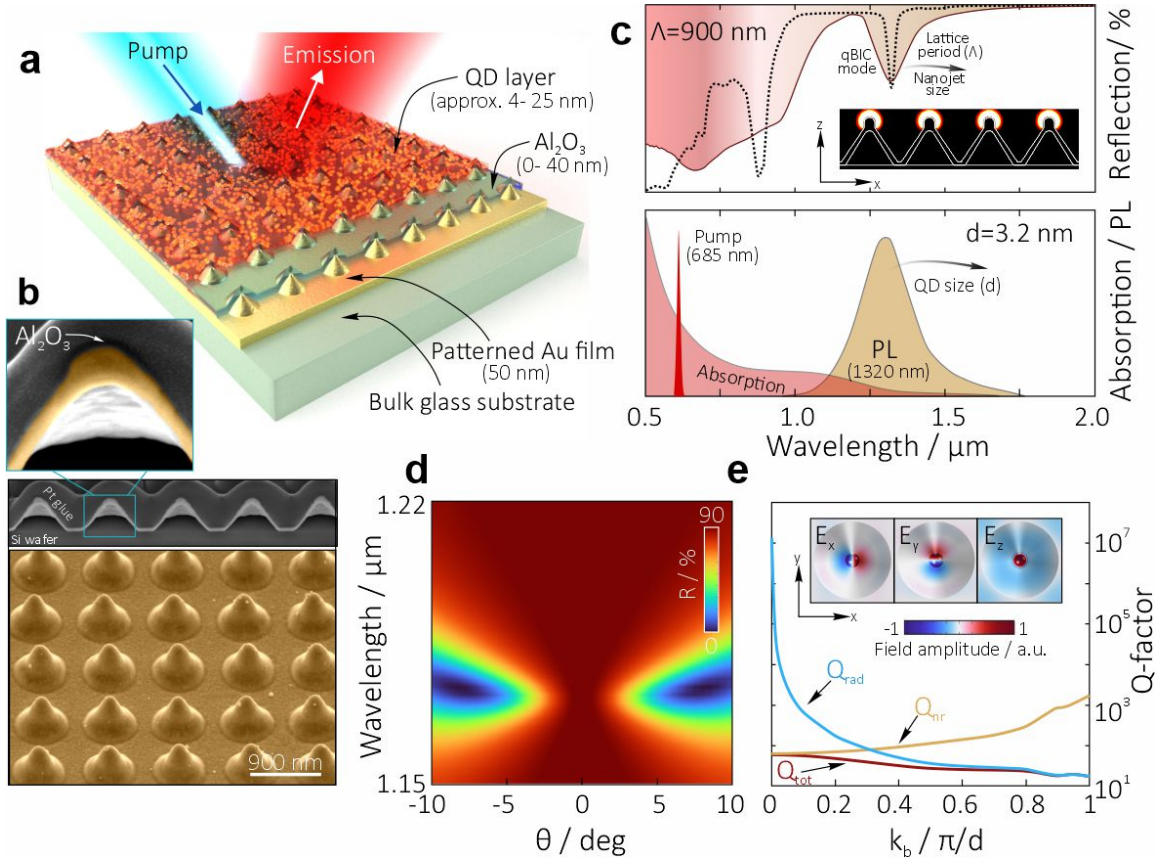

Figure 1. (a) Sketch of the structure under study: a layer of near-IR emitting HgTe QDs deposited on top of the qBIC-supporting plasmonic metasurface, comprising gold nanobumps arranged in a square-shaped lattice. A uniform dielectric Al_2O_3 film (varying from 0 to 40 nm in thickness) separates the QDs from the nanobumps. (b) Representative tilt-view (45°) SEM image of the laser-printed plasmonic metasurface, consisting of identical hollow nanobumps arranged in a square-shaped lattice with a period Λ = 900 nm. The top insets provide SEM images of a cross-section FIB cut, revealing the hollow geometry of the nanobump and the continuous Al_2O_3 spacer layer deposited on top. (c) Absorption and PL spectra of the HgTe QDs with an average size d = 3.2 nm (bottom panel) and measured (colored area) and calculated (black curve) reflection spectra of the plasmonic metasurface (top panel). The inset in the top panel provides a normalized EM-field amplitude (E/E_0) in the vicinity of the metasurface under BIC excitation at λ_R = 1320 nm, where E_0 is the incident field amplitude. (d) Calculated reflection spectrum of the plasmonic metasurface (Al_2O_3 spacer thickness 10 nm, Λ = 900 nm) as a function of the incidence angle θ of the excitation plane wave. (e) Calculated Brillouin zone dependence of the radiative (Q_{rad}), nonradiative (Q_{nr}), and total (Q_{tot}) quality factors of the BIC. Insets illustrate the distribution of the electric field components of the Γ-point BIC on the surface of the nanobump (top view) at λ_R = 1320 nm (Al_2O_3 spacer thickness 10 nm, Λ = 900 nm); k_b is the Bloch wavenumber.

The increase of the radiative Q-factor leads to an increase in the overall Q-factor of the BIC mode, making the latter efficient for enhancing the QD emission. While the excitation of the BICs under normal incidence is suppressed due to their nature, in realistic experimental conditions, there is a particular angular divergence of the beam which allows coupling to the BIC close to the Γ-point, where the quasi-BIC condition is fulfilled. The measured spectral response is limited by both nonradiative and radiative losses, resulting in the detected values $\Delta\lambda/\lambda_R \approx 11$ ($\Delta\lambda$ is the experimentally measured full width at half maximum (FWHM) value of the BIC resonant dip). To simulate the experimental conditions, we performed numerical modelling of the nanobumps with their hollow geometry retrieved from the FIB cross-section cuts (as demonstrated in the inset in Figure 1b) and averaged the reflectance spectra over angles slightly varied around the normal directions. The calculated reflection spectrum of the plasmonic metasurface (dashed curve, Figure 1c) demonstrates good agreement with the measured spectrum (colored area in top panel, Figure 1c) regarding the spectral position of the BIC mode. However, its simulated Q-factor is expectedly larger due to the presence of defects and material losses in the real laser-printed plasmonic metasurface. An additional factor leading to the spectral widening of the experimentally measured qBIC reflection dip apparently arises from the use of high-NA optics for FTIR signal collection. In particular, the efficiency of BIC excitation was found to be suppressed by the presence of wavevectors with non-normal incidence directions in the focal plane of the high-NA objective used for excitation/collection of the spectral signal.[9]

We then investigated the emission properties of HgTe QD layers with varying thickness *t*, placed directly on the qBIC-supporting plasmonic metasurface without any dielectric spacer layer, in the case of $\lambda_R = \lambda_{PL} = 1320$ nm (**Figure 2a**). Details of the deposition of the QD layers are given in the Supporting Information Section 1. A set of microscope objectives with variable NA = sin(θ) (where θ is the collection angle) was employed to measure the normalized PL signal as a function of *t*. The results of these measurements are summarized in Figure 2b, revealing the maximum enhancement (PL intensity from the HgTe QDs on a plasmonic Au metasurface normalized over the reference signal from the same thickness t layer capping a smooth Au film) for 15 nm thick QD layers, irrespective of the NA of the collecting objective.

For a monolayer of HgTe QDs, PL quenching is observed, emphasizing the importance of applying a dielectric spacer. For thicker HgTe QD layers, an enhancement mechanism based on the resonant coupling of QD emission with a qBIC mode was confirmed by the observed Purcell effect, e.g., reduction of the average radiative lifetime from $\langle\tau\rangle = 22.3$ ns to $\langle\tau\rangle = 4.0$ ns (Figure 2c, Figure S9, Table S1). Furthermore, the plasmon-mediated enhancement of the

electric field amplitude at the PL pump wavelength of 685 nm (Figure S7) and the bottom (quenched) QD layer acting as an effective dielectric spacer for the upper QD layers contribute to the observed emission enhancement.

For the HgTe QD layers with a thickness exceeding 15 nm, a decrease in PL intensity is observed, which is associated with an increase in the radiative lifetime to $\langle\tau\rangle$ = 10.97 ns (Figure 2c). This leads to a reduced efficiency of the near-field enhancement for the upper QD layers, an increasing mismatch between λ_R and λ_{PL} (Figure S4), and a strengthening of the nonradiative decay channels arising from non-resonant energy transfer between neighboring QDs.[13] Notably, the highest (up to 13-fold) PL enhancement was observed for the largest NA of the collecting optics, suggesting a modification of the emission directivity from the QD layer capping the plasmonic metasurface. This inference is also reflected from a comparison of the results of the emission directivity modelling of dipolar emitters capping the plasmonic metasurface (Figure 2d).

In accordance with the nature of the BIC mode, radiation in the direction normal to the surface is suppressed, as confirmed by the simulation results (far-field pattern in Figure 2d), and the maximal emission intensity is observed at approximately 20°. The emission intensity integrated over the collection angles from 0 to θ is depicted in Figure 2d by the gray line. Experimentally measured PL intensity data for various NAs corresponding to different collection angles are provided in Figure 2d by red circles, demonstrating good agreement with the simulation results and further corroborating the BIC nature of the resonant mode.

Taking into account the obtained results, we then focused on studying the emission from a monolayer (approximately 4 nm) of HgTe QDs coated on the BIC-supporting plasmonic metasurface, with an interposed dielectric Al_2O_3 spacer of variable (0 to 40 nm) thickness d (**Figure 3a**). For these experiments, we considered the linear redshift of λ_R upon increasing d (Figure S4) for each specific spacer thickness. Consequently, slightly different plasmonic arrays were fabricated in order to compensate for this shift to still ensure the best matching with the BIC mode at the emission maximum of HgTe QDs ($\lambda_R = \lambda_{PL}$).

Figure 3b (red circles) displays the normalized PL intensity of the HgTe QD monolayer as a function of the spacer thickness, revealing more than an order of magnitude stronger spontaneous emission at d = 10 nm. This observation confirms the deductions made from the analysis of the data in Figure 2b regarding the optimal spacer thickness (Figure S10, Table S2). Notably, the experimental data align well with the numerical simulation results shown in Figure 3b by the grey circles. In the simulations, point dipole sources were used in a finite array structure (see Experimental Section for details).

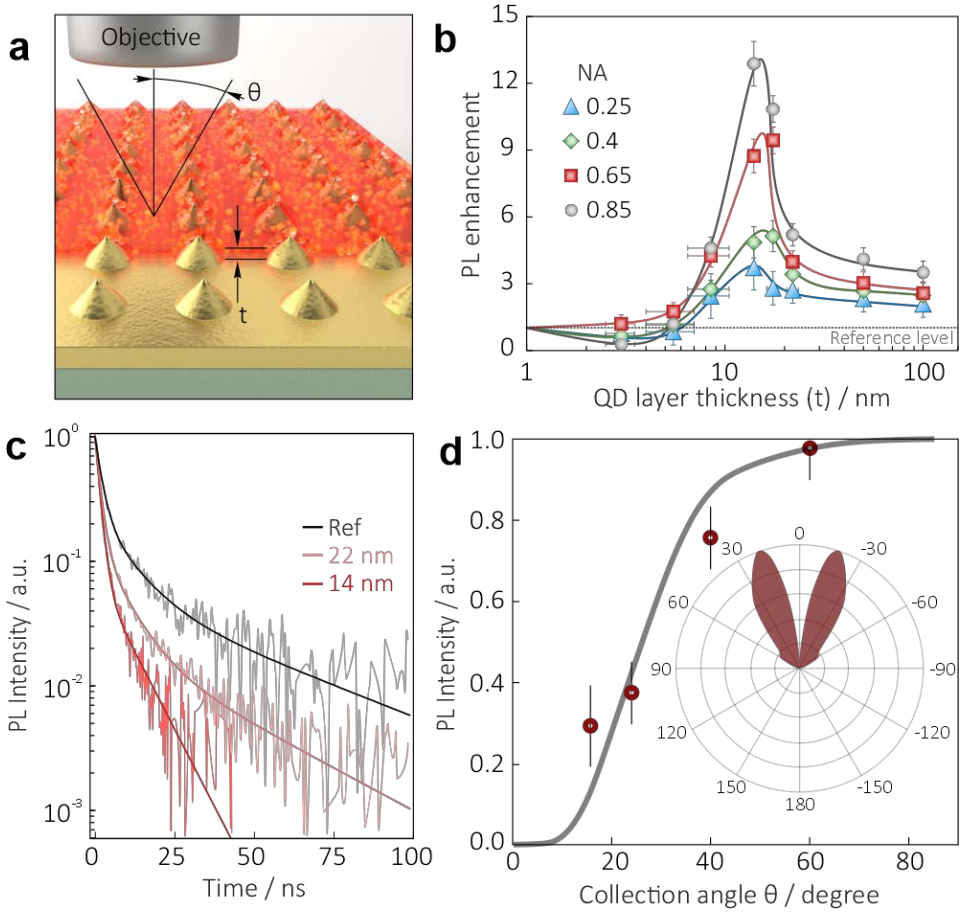

Figure 2. (a) Schematic illustration of the experimental measurement geometry. Emission from the HgTe QD layer of variable thickness *t*, capping the plasmonic metasurface, is collected by microscope objectives with a variable NA. (b) Normalized enhancement of the HgTe PL intensity as a function of the HgTe layer thickness *t*, measured at various NA. (c) PL decay curves measured from the HgTe QD layers with *t* = 14 nm and *t* = 22 nm capping the plasmonic metasurface. The black curve shows the reference PL decay for a 22-nm thick QD layer on a smooth Au surface. (d) Calculated (solid grey curve) and measured (red circles) normalized PL intensity as a function of the collection angle θ. The inset shows the calculated emission directivity diagram of the HgTe QDs on a plasmonic metasurface.

Furthermore, we investigated how the spectral detuning of the qBIC mode from the QD emission maximum affects the PL enhancement. To do this, plasmonic metasurfaces with varied nanobump geometry were fabricated, demonstrating a redshift of the resonance with the increase of the nanojet height (Figure 3d and Figure S8). Remarkably, in addition to the expected gradual reduction of the PL intensity for increasing mismatch between λ_{PL} and λ_R, we also detected modulation of the emission spectrum profile (Figure 3c and inset therein).

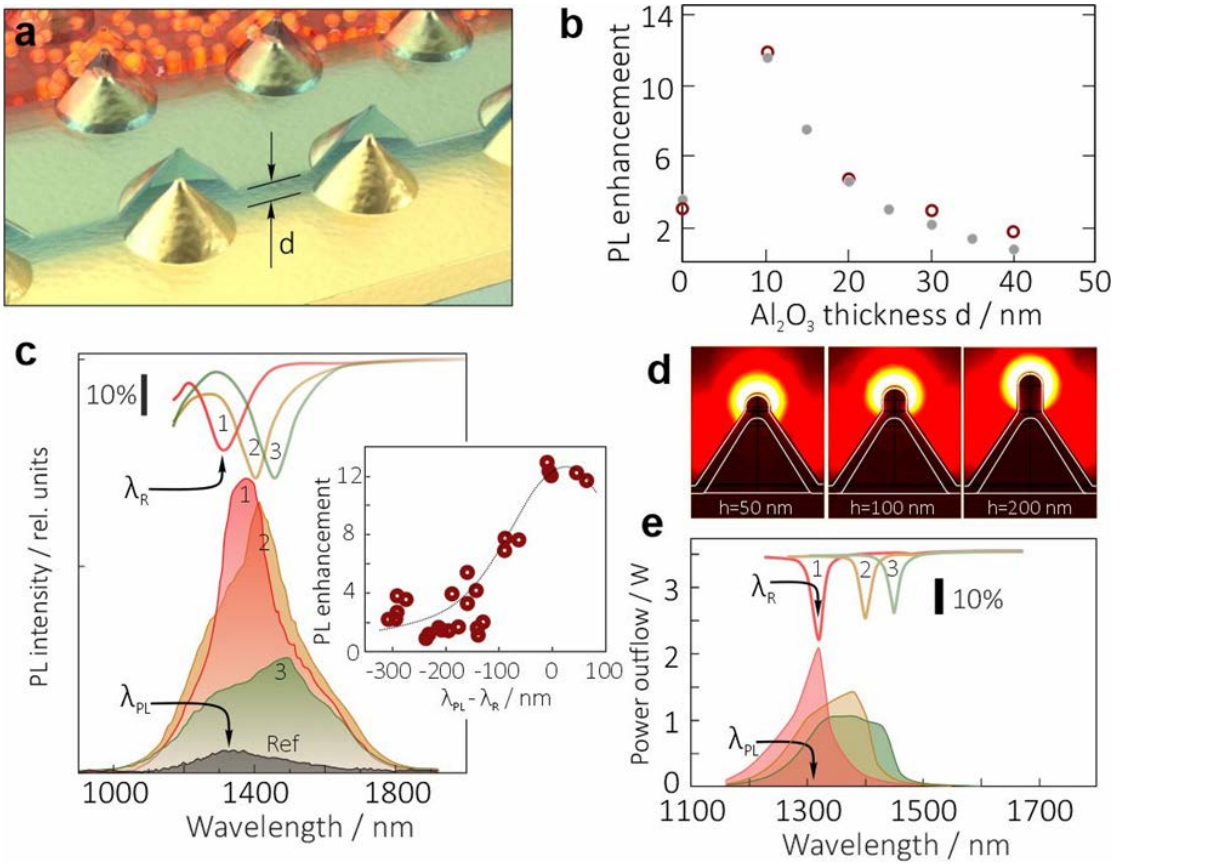

Figure 3. (a) Sketch of the considered geometry: a monolayer of HgTe QDs is separated from the qBIC-supporting plasmonic metasurface by an Al_2O_3 spacer with variable thickness *d* (0 to 40 nm). (b) Measured (red hollow circles) and calculated (grey circles) PL enhancement from the HgTe QD monolayer capping the plasmonic metasurface as a function of the Al_2O_3 spacer thickness *d*. (c) Series of PL spectra of the HgTe QD monolayer capping three metasurfaces (**Λ** = 900 nm, *d* = 10 nm) with varying positions of the BIC mode λ_R with respect to the emission maximum λ_{PL}. Experimentally measured reflection spectra of these metasurfaces are shown at the top of the panel. The inset shows the PL enhancement of the HgTe QD monolayer as a function of spectral detuning, λ_{PL}-λ_R, of the plasmon mode position with respect to the PL maximum. (d) EM field amplitude (E/E_0) in the vicinity of nanobumps with a fixed **Λ** = 900 nm and variable nanobump height (*h* = 50, 100, and 200 nm) at their qBIC mode wavelengths (λ_R = 1240, 1340, and 1540 nm, respectively). (e) Calculated shaping of the PL spectra of HgTe QDs capping the plasmonic metasurfaces with varying positions of the qBIC mode λ_R with respect to the emission maximum λ_{PL}. Corresponding calculated reflection spectra of these metasurfaces (Λ = 900 nm, *d* = 10 nm, and variable *h* = 92 (1), 134 (2), 158 nm (3)) are provided at the top of the panel.

Specifically, the spontaneous emission maximum follows the spectral position of the qBIC, as illustrated by a series of correlated PL and FTIR reflection spectra, resulting in a noticeable narrowing of the PL spectrum when $\lambda_R = \lambda_{PL}$. This PL shaping effect was not observed for thicker QD layers capping the plasmonic metasurface without a spacer (Figure 2b), indicating a much stronger plasmon-exciton interaction in the spacer-buffered structure containing a monolayer of QDs. We also should note that, according to the BIC mode field distribution shown in Figure 3d, the main contribution to PL intensity comes from the QDs located at the top of the nanojet where the local density of states is maximal.

To explain this behavior, we performed modelling of the PL emission for nanobumps with varied nanojet height (*h*). The simulations confirm that while the position of the QD's PL maximum is fixed at 1320 nm, the BIC resonance redshifts with the increase of *h*. The resulting PL spectrum is governed by the convolution of two overlapping bands: the PL spectrum of pristine QDs and the emission enhancement spectrum of the qBIC. Detuning of these two emission bands leads to the effective widening and suppression of the simulated PL spectra (Figure 3e), which is also observed in the experiment (Figure 3c). A similar behavior was observed for a plasmonic metasurface (Λ =1000 nm) with spacer thickness up to 40 nm capped with a monolayer of larger HgTe QDs (h_{QD} = 3.6 nm) with a PL maximum at the telecom wavelength of 1550 nm (Figure S11), further demonstrating the versatility of the proposed approach.

3. Conclusion

In conclusion, we have demonstrated efficient tuning of the PL intensity of near-IR emitting HgTe QDs coupled to a spacer-passivated plasmonic Au metasurface supporting BIC modes. Specifically, we achieved a narrowing of the PL spectrum of the coupled QD monolayer and more than an order of magnitude stronger spontaneous emission from the monolayer of QDs with their PL maximum spectrally matching the BIC resonance of the plasmonic metasurface. The observed PL enhancement and shaping effects were attributed to the Purcell effect, which is in agreement with the systematic experimental measurements and optical simulations. Considering that the qBIC-supporting plasmonic metasurface was produced using scalable direct fs-laser printing, the strategy we propose to tune the PL intensity and PL spectral shape of near-IR emitting QDs paves the way for the development of next-generation IR-emitting devices incorporating these structures.

4. Experimental Methods

Chemicals. Mercury (II) chloride (ACS, Sigma Aldrich), elemental tellurium (99.99%, Sigma Aldrich), 2-furanmethanethiol (FMT, 97%, Acros Organics), tripropylamine (TPA, 98%, Sigma Aldrich), dimethylformamide (DMF, ACS, Anaqua), ultrahigh-purity Ar gas (99.999%, Linde), 1-dodecanethiol (DDT, >98%, Sigma Aldrich), tetrachloroethylene (TCE, 99.5%, Aladdin Chemicals), dimethylsulfoxide (DMSO, 99.9%, Sigma Aldrich), ethyl acetate (ACS, Anaqua), n-hexane (ACS, Anaqua), methanol (ACS, Anaqua). All chemicals were used as received without further purification.

Synthesis of HgTe QDs. HgTe QDs were synthesized using a continuous-growth method in an aprotic organic solvent, as reported earlier.[3a] In a three-neck flask, 8 mmol (2.2 g) of $HgCl_2$ was dissolved in 100 mL of DMF, along with 2.4 mL of FMT ligand and 3 ml of TPA organic base. H_2Te gas, produced by an electrochemical cell (65% concentrated phosphoric acid as electrolyte, platinum wire as anode, and fused elemental tellurium as cathode) at a current of 300 mA, was used as an anion precursor source. The electrochemical cell and the reaction flask were deaerated with a flow of ultra-high-purity Ar gas for one hour. The temperature of the solution in the reaction flask was set at -13 °C. H_2Te gas, buffered in a flow of Ar, was passed into the solution for 40 min, and the temperature was then gradually (0.5 °C/min) raised to 25 °C to ensure the formation of HgTe QDs. The solution was kept at 25 °C for 1 and 1.5 h to grow the QDs to the desired sizes of 3.2 and 3.6 nm.

QD aliquots were precipitated with ethyl acetate and hexane (QD:ethyl acetate:hexane v/v ratio 1:2.5:1), centrifuged, and the precipitate was dried under a nitrogen gas flow. The QDs were redissolved in DMSO and set to ligand exchange (FMT to DDT) during the liquid phase transfer into an IR-transparent solvent (from DMSO to TCE). The resulting DDT-capped HgTe QDs were carefully washed with methanol several times and purged with dry nitrogen gas. For IR spectroscopy, the HgTe QDs were finally redissolved in 3 mL of TCE.

Characterization. Transmission electron microscopy (TEM) was performed using a JEOL JEM-2100F microscope with an accelerating voltage of 200 keV. HgTe QDs were deposited from a toluene solution onto a copper grid covered with an ultra-thin amorphous carbon layer. X-ray diffraction (XRD) patterns were recorded in Bragg-Brentano geometry on a Rigaku SmartLab 9kW diffractometer using $CuK_{\alpha 1,2}$ irradiation in the range of 2θ from 15 to 85 degrees, with a step size of 0.01 degree and a scan rate of 1.5 deg/min. X-ray photoemission spectroscopy (XPS) was conducted using a ThermoFisher X-ray photoelectron spectrometer. The pass energy varied from 20 to 100 eV, and the data were collected from a uniform area (free from periodic structures) with a diameter of 500 µm. The spectra were normalized to the Shirley function

background, and the photoionization cross-section of each component was considered when calculating atomic ratios.

Absorption spectra of the diluted HgTe QD solutions in TCE (360-2500 nm range) or DMF (360-1200 nm range) were collected on a 3600i Plus UV-IR (Shimadzu) spectrometer. The concentration of QDs, converted from the number of [Hg^{2+}] atoms (both in DMF straight after synthesis and after extraction into TCE), was determined from the absorption at 415 nm.[14a] PL spectra were recorded on an FLS920 (Edinburgh Instruments) spectrometer equipped with a liquid-nitrogen-cooled NIR PMT and an InSb photodiode. A 685 nm steady-state laser was used as the excitation source. The average size was estimated using PL peak-size curves for HgTe QDs.[14b, 14c]

Optical absorption and PL spectra were collected from plasmonic arrays with deposited QDs using a purpose-built confocal setup compatible with both the 3600i Plus UV-IR and FLS920 spectrometers. The light from the spectrometer was focused on the array using different-NA apochromatic microscope objectives from Newport. The light collected from the sample was reflected to the spectrometer's detection path by using a 50:50 beam-splitting plate for absorption measurements, or a 45° 1100-nm short pass filter for PL measurements Additionally, the collected light was collimated with an apochromatic lens to match the F-number of the detector's monochromator.

Time-resolved photoluminescence (TRPL) studies were carried out on a non-commercial, purpose-built micro-PL setup. Output light from a tunable mode-locked Ti:Sapphire femtosecond oscillator (Coherent Mira900; <130 fs pulse width, 76 MHz repetition rate, 720 nm central wavelength) was pulse-picked down to a 500 kHz pulse rate, and the maximal pulse fluence was equal to 10 μJ/cm^2. For PL excitation and collection, the same microscope objectives and filters as in the steady-state measurements were used. The PL signal from the sample was collimated and directed to the input of a fiber-coupled infrared photon detection module based on a cooled InGaAs/InP single-photon avalanche photodiode (MPD, PDM-IR) and acquired with PicoQuant TimeHarp 260 card. The overall emission from the deposited QD layers was rather weak, and therefore, the photon hit-rate did not exceed 0.25%, ensuring operation in a single-photon counting mode. On the other hand, a sufficient signal-to-noise ratio was achieved only in the first 150 ns for a signal collection time of 100 s. Longer collection times could provide a better signal at longer times after photoexcitation, but this may also cause undesirable QD photo-charging, introducing an additional non-radiative decay channel. Thus, a 100 s collection time limit was used as a necessary trade-off. We note that a weak long decay

time component most likely exists in the HgTe QD transient PL profile, but its relative contribution would be small, and its presence does not affect the key findings of this study.

Fabrication of the BIC supporting metasurface. The BIC supporting metasurface was fabricated by combination of an inexpensive and scalable magnetron sputtering of thin Au films with a direct fs-laser printing technique. First, a gold film with a thickness of 50 nm was coated over a glass substrate using magnetron deposition. Then, laser patterning of the glass-supported Au films was carried out using ~200 fs second-harmonic (λ = 515 nm) pulses generated by a regeneratively amplified Yb:KGW laser system (Pharos, Light Conversion) at 50 kHz repetition rate. Output laser radiation with a Gaussian-shaped lateral intensity profile was focused onto the Au film surface by a microscope objective (50x, Mitutoyo) with a numerical aperture NA=0.42. A computer-driven nanopositioning platform (ANT130XY, Aerotech) ensured precise (position deviation less than 100 nm) movement of the sample surface with respect to the laser focal spot, allowing each pulse to form isolated nanobumps arranged into a square-shaped lattice with a period (**Λ**) defined by the sample scanning speed. The described approach provided good reproducibility of the qBIC mode position and its amplitude upon cyclic fabrication (Figure S12). Finally, a dielectric Al_2O_3 layer of variable thickness (ranging from 10 to 40 nm) was deposited over the laser-printed metasurface using magnetron sputtering. Scanning electron microscopy (SEM) was carried out to check the surface morphology of the produced device at every fabrication step.

Numerical modelling. The modelling of the optical properties of the plasmonic structures and the QD emission enhancement in the vicinity of the metasurface was carried out using commercially available software, COMSOL Multiphysics. The metasurface mode analysis and reflectance spectra calculations were performed for a periodic structure, while the simulations of PL enhancement were done for a metasurface of a finite size, with point dipoles used as light sources. This approach is a well-established method for modelling a quantum emitter's interactions with metasurfaces,[15a] and simulations showed that the convergence of the obtained results was observed for a square 5x5 array of nanojets. We have simulated the far-field radiation pattern by averaging over the quantum emitters' spatial location and orientation along the *x*-, *y*-, and *z*-axes. Due to the fact that the radiation pattern is not symmetrical with respect to azimuthal numbers, additional patterning was used. Finally, to interpret the peculiarities in the modelled spectra, we performed an eigenmode analysis of both single plasmonic structures and the modes of the metasurface. Dispersion spectra of gold and aluminum oxide were taken from Refs.[15b] and [15c], respectively. Characteristic linear sizes of the Au nanojets were chosen

in accordance with dimensions observed in SEM data: the cone height was 600 nm, the height of the nanojets varied from 0 to 320 nm, and the bottom radius of the cone was 300 nm.

Supporting Information

Supporting Information is available from the Wiley Online Library or from the author.

Acknowledgements

We acknowledge financial support from the Research Grants Council of Hong Kong SAR (CRF C7035-20G, and 16304722), and the Innovation and Technology Commission of Hong Kong SAR (ITS/027/22MX). The experiments (fabrication of the BIC metasurface, optical characterization and PL measurements) were carried out within the Russian Science Foundation project 21-79-10197, the numerical simulations were supported by Russian Science Foundation project 21-72-10107. The work was also supported by the Program Priority 2030.

Received: ((will be filled in by the editorial staff))

Revised: ((will be filled in by the editorial staff))

Published online: ((will be filled in by the editorial staff))

References

[1] a) A. L. Rogach, *Semiconductor Nanocrystal Quantum Dots: Synthesis, Assembly, Spectroscopy and Applications*, Springer-Verlag/Wien, New York, USA **2008**; b) (2) Y. Tian, H. Luo, M. Chen, C. Li, S. V. Kershaw, R. Zhang, A. L. Rogach, *Nanoscale* **2023**, 15, 6476-6504.

[2] a) B. Zhu, M. Chen, Q. Zhu, G. Zhou, N. M. Abdelazim, W. Zhou, S. V. Kershaw, A. L. Rogach, N. Zhao, H. K. Tsang, *Adv. Mater. Technol*. **2019**, 4, 1900354; b) C. Gréboval, A. Chu, N. Goubet, C. Livache, S. Ithurria, E. Lhuillier, *Chem. Rev*. **2021**, 121, 3627–3700; c) X. Shen, J. C. Peterson, P. Guyot-Sionnest, *ACS Nano* **2022**, 16, 7301–7308.

[3] a) S. V. Kershaw, W. K. Yiu, A. Sergeev, A. L. Rogach, *Chem. Mater*. **2020**, 32, 3930–3943; b) S.-S. Chee, C. Gréboval, D. V. Magalhaes, J. Ramade, A. Chu, J. Qu, P. Rastogi, A. Khalili, T. H. Dang, C. Dabard, Y. Prado, G. Patriarche, J. Chaste, M. Rosticher, S. Bals, C. Delerue, E. Lhuillier, *Nano Lett*. **2021**, 21, 4145– 4151; c) P. Guyot-Sionnest, M. M. Ackerman, X. Tang, *J. Chem. Phys*. **2019**, 151, 060901; d) H. Zhang, J. C. Peterson, P. Guyot-Sionnest, *ACS Nano* **2023**, 17, 8, 7530–7538; e) B. T. Diroll, B. Guzelturk, H. Po, C. Dabard, N. Fu, L. Makke, E. Lhuillier, S. Ithurria, S. *Chem. Rev*. **2023**, 123(7), 3543-3624; f) Y. Dong, M. Chen, W. K. Yiu, Q. Zhu, G. Zhou, S. V. Kershaw, N. Ke, C. P. Wong, A. L. Rogach, N. Zhao, *Adv. Sci*. **2020**, 7, 2000068.

[4] a) X. Tang, M. M. Ackerman, G. Shen, P. Guyot-Sionnest, *Small* **2019**, 15, 1804920; b) E. Bossavit, J. Qu, C. Abadie, C. Dabard, C. T. Dang, E. Izquierdo, A. Khalili, C. Gréboval, A. Chu, S. Pierini, M. Cavallo, Y. Prado, V. Parahyba, X. Z. Xu, A. Decamps-Mandine, M. Silly, S. Ithurria, E. Lhuillier, *Adv. Opt. Mat.* **2022**, 10, 2101755; c) T. H. Dang, C. Abadie, A. Khalili, C. Gréboval, H. Zhang, Y. Prado, X. Z. Xu, D. Gacemi, A. Descamps-Mandine, S. Ithurria, Y. Todorov, C. Sirtori, A. Vasanelli, E. Lhuillier, *Adv. Opt. Mat*. **2022**, 10, 2200297, d) T. Dang, A. Khalili, C. Abadie, C. Gréboval, M. Cavallo, H. Zhang, E. Bossavit, J. K. Utterback, E. Dandeu, Y. Prado, G. Vincent, S. Ithurria, Y. Todorov, C. Sirtori, A. Vasanelli, E. Lhuillier, *ACS Photonics*, **2022**, 9, 2528–2535; e) Y. Luo, S. Zhang, X. Tang, M. Chen, *J. Mater. Chem. C*, **2022**, 10, 8218-8225.

[5] a) B. Ji, E. Giovanelli, B. Habert, P. Spinicelli, M. Nasilowski, X. Xu, N. Lequeux, J.-P. Hugonin, F. Marquier, J.-J. Greffet, B. Dubertret, *Nat. Nanotechnol*. **2015**, 10 (2) 170– 175; b) Z. Tian, M. Zhang, X. Wang, Q. Li, Y. Li, F. Yun, S. W. Ricky Lee, *J. Appl. Phys.* **2023**, 133(12), 124901; c) Y. Park, H. Kim, J.-Y. Lee, W. Ko, K. Bae, K.-S. Cho, *Nanophotonics* **2020**, 9(5), 1023-1030; d) L. Ma, P. Yu, W. Wang, H. Kuo, A. O. Govorov, S. Sun, Z. Wang, *Laser Photon. Rev*. **2021**, 15 (5), 2000367; e) V. Krivenkov, D. Dyagileva, P. Samokhvalov, I. Nabiev, Y. Rakovich, *Annal. der Phys.* **2020**, 532 (8), 2000236.

[6] a) K. Yang, X. Yao, B. Liu, B. Ren, *Adv. Mater*. **2021**, e2007988; b) A. A. Sergeev, D. V. Pavlov, A. A. Kuchmizhak, M. V. Lapine, W. K. Yiu, Y. Dong, N. Ke, S. Juodkazis, N. Zhao, S. V. Kershaw, A. L. Rogach, *Light: Sci. Appl*. **2020**, 9, 16; c) M. Chen, L. Lu, H. Yu, C. Li, N. Zhao, *Adv. Sci*. **2021**, 8, 2101560; d) B. Kalinic, T. Cesca, I. G. Balasa, M. Trevisani, A. Jacassi, S. A. Maier, R. Sapienza, G. Mattei, *ACS Photonics* **2023**, 10, 2, 534–543.

[7] a) C. W. Hsu, B. Zhen, A. D. Stone, J. D. Joannopoulos, M. Soljačić, *Nat. Rev. Mater*. **2016**, 1, 16048; b) B. Zhen, C. W. Hsu, L. Lu, A. D. Stone, M. Soljačić, *Phys. Rev. Lett*. **2014**, 113, 2574011; c) S.I. Azzam, A.V. Kildishev, *Adv. Opt. Mater*. **2021**, 9, 2001469; d) K. Koshelev, G. Favraud, A. Bogdanov, Y. Kivshar, A. Fratalocchi, *Nanophotonics* **2019**, 8, 725–745.

[8] a) F. Yesilkoy, E. R. Arvelo, Y. Jahani, M. Liu, A. Tittl, V. Cevher, Y. Kivshar, H. Altug, *Nat. Photonics* **2019**, 13, 390– 396; b) A. Tittl, A. Leitis, M. Liu, F. Yesilkoy, D.-Y. Choi, D. N. Neshev, Y. S. Kivshar, H. Altug, *Science* **2018**, 360, 1105– 1109; c) S. T. Ha, Y. H. Fu, N. K. Emani, Z. Pan, R. M. Bakker, R. Paniagua-Dominguez, A. I. Kuznetsov, *Nat. Nanotechnol*. **2018**, 13 (11), 1042; d) Z. Liu, Y. Xu, Y. Lin, J. Xiang, T. Feng, Q. Cao, J. Li, S. Lan, J. Liu, *Phys. Rev. Lett*. **2019**, 123, 253901; e) M. Minkov, D. Gerace, S. Fan, *Optica* **2019**, 6, 1039–1045; f) E. Mikheeva, K. Koshelev, D.-Y. Choi, S. Kruk, J. Lumeau, R. Abdeddaim, I. Voznyuk, S. Enoch, Y. Kivshar, *Opt. Express* **2019**, 27, 33847–33853.

[9] a) Y. Liang, H. Lin, S. Lin, J. Wu, W. Li, F. Meng, Y. Yang, X. Huang, B. Jia, Y. Kivshar, *Nano Lett*. **2021**, 21 (20), 8917–8923; b) Y. Liang, K. Koshelev, F. Zhang, H. Lin, S. Lin, J. Wu, B. Jia, Y. Kivshar, *Nano Lett*. **2020**, 20 (9), 6351–6356; c) A. Aigner, A. Tittl, J. Wang, T. Weber, Y. Kivshar, S.A. Maier, H. Ren. *Sci. Adv*. **2022**, 8, eadd4816.

[10] a) Y. Nakata, T. Okada, M. Maeda, *Jpn. J. Appl. Phys*. **2003**, 42, L1452– L1454; b) D. Pavlov, S. Syubaev, A. Kuchmizhak, S. Gurbatov, O. Vitrik, E. Modin, S. Kudryashov, X. Wang, S. Juodkazis, M. Lapine, *Appl. Surf. Sci*. **2019**, 469, 514–520; c) A. A. Kuchmizhak, A. P. Porfirev, D. Pavlov, M. Lapine, O. B. Vitrik, P. A. Danilov, S. Gurbatov, S. A. Kulinich, S. I. Kudryashov, S. N. Khonina, *Opt. Lett*. **2019**, 44, 283–286; d) E. Stankevičius, K. Vilkevičius, M. Gedvilas, E. Bužavaitė-Vertelienė, A. Selskis, Z. Balevičius, *Adv. Opt. Mat*. **2021**, 9(12), 2100027.

[11] a) D. Pavlov, A. Zhizhchenko, L. Pan, A. A. Kuchmizhak, *Materials* **2022**, 15(5), 1834; b) K. Vilkevičius, A. Selskis, E. Stankevičius, *Appl. Surf. Sci*. **2023**, 617, 156629.

[12] Z. Sadrieva, K. Frizyuk, M. Petrov, Y. Kivshar, A. Bogdanov, *Phys. Rev. B: Condens. Matter Mater. Phys*. **2019**, 100, 115303.

[13] K.A. Sergeeva, K. Fan, A. A. Sergeev, S. Hu, H. Liu, C.C. Chan, S. V. Kershaw, K. S. Wong, A. L. Rogach, *J. Phys. Chem. C* **2022**,126(45) 19229-19239.

[14] a) E. Lhuillier, S. Keuleyan, P. Guyot-Sionnest, *Nanotechnology* **2012**, 23, 175705; b) M. V. Kovalenko, E. Kaufmann, D. Pachinger, J. Roither, M. Huber, J. Stangl, G. Hesser, F. Schäffler, W. Heiss, *J. Am. Chem. Soc*. **2006**, 128 (11), 3516–3517; c) T. Aubert, A. A. Golovatenko, M. Samoli, L. Lermusiaux, T. Zinn, B. Abécassis, A. V. Rodina, Z. Hens, *Nano Lett.* **2022**, 22 (4), 1778–1785.

[15] a) A. Vaskin, R. Kolkowski, A. F. Koenderink, I. Staude, *Nanophotonics* **2019**, 8, 1151–1198; b) P. B. Johnson, R. W. Christy, *Phys. Rev. B: Condens. Matter Mater. Phys*. **1972**, 6, 4370; (c) A. K. Harman, S. Ninomiya, S. Adachi, *J. Appl. Phys*. **1994**, 76, 8032.

Table of content

Kseniia A. Sergeeva, Dmitrii V. Pavlov, Albert A. Seredin, Eugeny V. Mitsai, Aleksandr A. Sergeev, Evgeny B. Modin, Anastasiia V. Sokolova, Tsz Chun Lau, Kseniia V. Baryshnikova, Mihail I. Petrov, Stephen V. Kershaw, Aleksandr A. Kuchmizhak, Kam Sing Wong, Andrey L. Rogach

Laser-printed plasmonic metasurface supporting bound states in the continuum enhances and shapes infrared spontaneous emission of coupled HgTe quantum dots

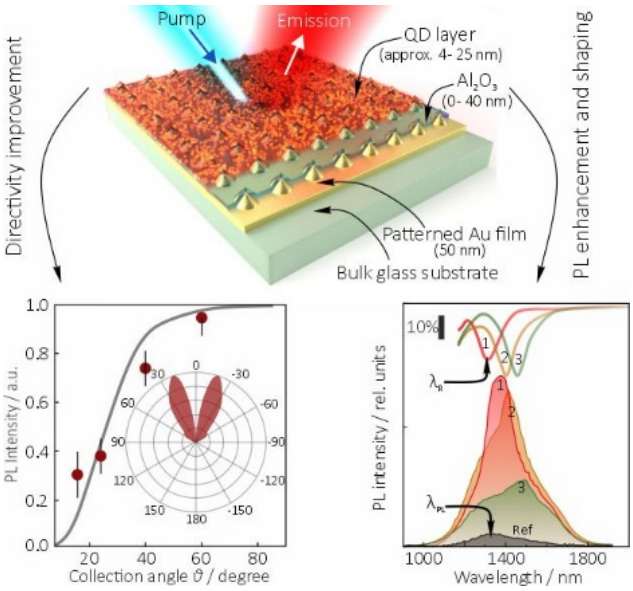

In this work, we couple near-infrared emitting HgTe quantum dots to plasmonic metasurfaces supporting quasi-bounded state in the continuum modes, which efficiently tune the output emission from the quantum dot monolayer. A 12-fold enhancement in photoluminescence is observed, with controllable emission spectra shaping and improved directivity due to the Purcell effect, as corroborated by systematic optical measurements and optical simulations.